

BUCKLING OF ELASTIC-PLASTIC SHELLS OF REVOLUTION WITH DISCRETE ELASTIC-PLASTIC RING STIFFENERS†

DAVID BUSHNELL‡

Lockheed Palo Alto Research Laboratory, 3251 Hanover Street, Palo Alto, CA 94304, U.S.A.

(Received 22 January 1975; revised 4 June 1975)

Abstract—The theory is summarized for axisymmetric prebuckling and nonsymmetric bifurcation buckling of ring-stiffened shells of revolution. The analysis is based on finite difference energy minimization in which moderately large meridional rotations, elastic-plastic effects, and primary or secondary creep are included. This theory is implemented in a computer program called BOSOR5, for the analysis of segmented and branched ring-stiffened shells of revolution of multi-material construction.

Comparisons between test and theory are given for axisymmetric collapse and nonsymmetric bifurcation buckling of 69 machined ring-stiffened aluminum cylinders submitted to external hydrostatic pressure. Because most of the cylinders fail at an average stress which corresponds to the knee of the stress-strain curve, the analytical predictions are not very sensitive to modeling particulars such as nodal point density or boundary conditions. Agreement between test and theory is improved if the analytical model reflects the fact that the shell and rings intersect over finite axial lengths.

NOTATION

- A Pertains to cross-section area of ring
- $[C]$ Matrix defined in eqn (5)
- C_r See eqn (5)
- $[D]$ $[D] = \frac{E}{1-\nu^2} \begin{bmatrix} 1 & \nu \\ \nu & 1 \end{bmatrix}$
- E Young's modulus
- E_T Tangent modulus
- ϵ Strain anywhere in shell wall or in the ring cross-section
- H' $H' = EE_T/(E - E_T)$
- H Radial force/length, applied at ring centroid, positive outward (Fig. 2)
- M Meridional moment about ring centroid, positive clockwise (Fig. 2)
- M Number of degrees of freedom in the nonsymmetric bifurcation buckling analysis
- n Number of circumferential waves in the buckling pattern
- N Number of degrees of freedom in the axisymmetric prebuckling analysis
- p_1, p_2, p_3 Meridional, circumferential, normal tractions
- q Nodal point degree of freedom
- r Radius from axis of revolution to any point in shell wall or in ring cross-section
- R_1, R_2 Normal meridional, circumferential radii of curvature
- s Arc length along shell reference surface (Fig. 3)
- S In-plane shear force/length acting along ring centroidal axis
- u Meridional displacement of point on shell reference surface (Fig. 3)
- u^* Axial displacement of point on shell reference surface (Fig. 3)
- U Strain energy
- v, v^* Circumferential displacement of point on shell reference surface
- V Axial load/length applied to ring centroid (Fig. 2), or volume depending on context
- w Normal outward displacement of point on shell reference surface (Fig. 3)
- w^* Radial displacement of point on shell reference surface (Fig. 3)
- z Coordinate normal to shell wall reference surface
- ν Poisson's ratio
- ψ Gradient of energy functional
- $\sigma, \bar{\sigma}$ Stress, effective stress
- θ Circumferential coordinate
- χ Meridional rotation

Subscripts

- b Infinitesimal buckling quantity
- c Pertains to ring centroid
- 1 Meridional
- 2 Circumferential
- 0 Prebuckling quantity, or quantity as of last update
- i i th degree of freedom

†This study was sponsored by the Lockheed Independent Research Program.

‡Staff Scientist.

r Pertains to ring
s Pertains to ring shear center
T Tangent modulus

Superscripts

b Infinitesimal buckling quantity
P Plastic
C Creep
T Thermal or transpose, depending on context

Symbols

[] Row vector
{ } Column vector
[] Matrix

INTRODUCTION

In [1] and [2] the nonlinear prebuckling and bifurcation buckling analyses of elastic-plastic shells of revolution are described. A computer program called BOSOR5 has been written [3] based on the analyses in [1] and [2]. BOSOR5 also treats shells with elastic-plastic discrete ring stiffeners. The purpose of this paper is to give a brief outline of the analysis including the discrete rings and to present a comparison with test results on ring-stiffened cylinders obtained by Boichot and Reynolds [4] in 1965. The details of the analysis of the discrete rings are given in Section 3 of Vol. III of [3].

Previous work on elastic-plastic instability of ring-stiffened shells is apparently limited to cylinders [5–9]. The most recent paper is by Lee [8], who used the Rayleigh–Ritz method.

The analysis here is based on energy minimization in which the displacement and rotation of any ring cross-section are related to those of the shell reference surface at the ring attachment point by simple expressions: plane sections of the ring cross-section are assumed to remain plane as the ring deforms, with the planar rotations being identified as those along the axis of shear centers of the ring.

BASIC EQUATIONS

The analysis is based on the principle of virtual work:

$$\delta U = \int_{\text{Volume}} [\epsilon - \epsilon^P - \epsilon^C - \epsilon^T] [D] \{\delta\epsilon\} dV = \delta W. \quad (1)$$

If the structure is composed of shells of revolution and rings, eqn (1) can be written in the form

$$\begin{aligned} \delta U - \delta W = & \int_{\theta} \left[\int_s \int_z [\epsilon - \epsilon^P - \epsilon^C - \epsilon^T] [D] \{\delta\epsilon\} r dz ds \right] \text{ Shell strain energy} \\ & + \int_A (\epsilon_r - \epsilon_r^P - \epsilon_r^C - \epsilon_r^T) E_r \delta\epsilon_r r dA \quad \text{Ring strain energy} \\ & - \int_s \left[(p_1 \delta u + p_2 \delta v + p_3 \delta w) - p_3 \left(\frac{1}{R_1} + \frac{1}{R_2} \right) w \delta w \right. \\ & \left. + p_3 \left(\frac{u \delta u}{R_1} + \frac{v \delta v}{R_2} \right) + \frac{dp_3}{ds} (u \delta w + w \delta u) \right] r ds \quad \text{External forces on shell} \\ & - (-V \delta u_c + S \delta v_c + H \delta w_c + M \delta \chi) r_c \Big] d\theta. \quad \text{External forces on ring} \quad (2) \end{aligned}$$

The nonlinear terms multiplied by p_3 are taken from [10] and represent the pressure-rotation effect.

The total strains ϵ in the shell can be expressed in terms of reference surface strains and changes in curvature, and these reference surface quantities can then be expressed, through appropriate finite difference expressions, in terms of the nodal point displacements q_i shown in Fig. 1. The u_i , v_i and w_i are meridional, circumferential and normal displacement components, respectively. Moderately large prebuckling meridional rotations are permitted.

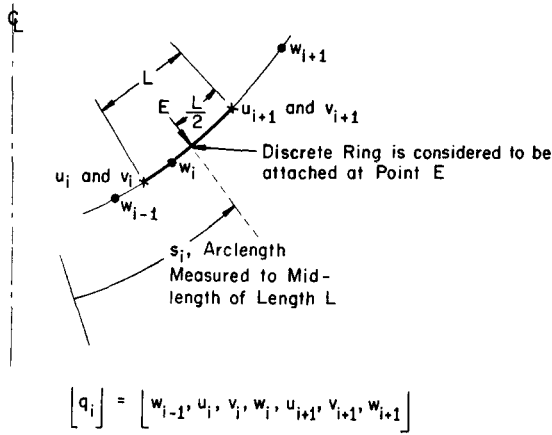


Fig. 1. Locations of shell nodal point variables $[q_i]$ associated with displacement and rotation of a discrete ring attachment point. The ring energy will ultimately be expressed in terms of these variables.

The ring theory is based on the assumption that plane sections of the ring remain plane, with the origin for rotations of this plane being the shear center of the ring cross-section. The total strain ϵ_r anywhere in the ring cross-section can thus be expressed in terms of displacement components u_s, v_s, w_s of the ring shear center and rotation χ about the ring shear center. The components u_s, v_s, w_s and the components of ring centroidal displacements u_c, v_c, w_c shown in Fig. 2, can be expressed in terms of the displacement components u^*, v, w^* of the circumferential line on the shell reference surface to which the ring is considered to be attached (Fig. 3). These components are easily written in terms of u, v, w and then expressed in terms of the nodal point variables q_i shown in Fig. 1.

The expressions used in the various transformations described above are given in [1] and [2] for the shell and in [3] for the ring. In order to save space they will not be repeated here.

PREBUCKLING ANALYSIS

For equilibrium

$$\begin{aligned}
 \frac{\partial(U-W)}{\partial q_i} = \psi_i = & \int_{\theta} \left[\int_s \int_z [\epsilon - \epsilon^P - \epsilon^C - \epsilon^T] [D] \left\{ \frac{\partial \epsilon}{\partial q_i} \right\} r dz ds \right. \\
 & + \int_A (\epsilon_r - \epsilon_r^P - \epsilon_r^C - \epsilon_r^T) E_r \frac{\partial \epsilon_r}{\partial q_i} r dA \\
 & - \int_s \left[\left(p_1 \frac{\partial u}{\partial q_i} + p_2 \frac{\partial v}{\partial q_i} + p_3 \frac{\partial w}{\partial q_i} \right) - p_3 \left(\frac{1}{R_1} + \frac{1}{R_2} \right) w \frac{\partial w}{\partial q_i} \right. \\
 & \left. + p_3 \left(\frac{u}{R_1} \frac{\partial u}{\partial q_i} + \frac{v}{R_2} \frac{\partial v}{\partial q_i} \right) + \frac{dp_3}{ds} \left(u \frac{\partial w}{\partial q_i} + w \frac{\partial u}{\partial q_i} \right) \right] r ds \\
 & \left. - \left(-V \frac{\partial u_c}{\partial q_i} + S \frac{\partial v_c}{\partial q_i} + \frac{\partial w_c}{\partial q_i} + M \frac{\partial \chi}{\partial q_i} \right) r_c \right] d\theta = 0. \quad (3)
 \end{aligned}$$

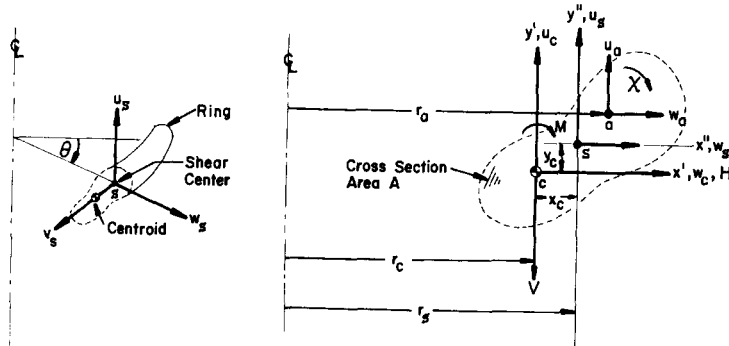


Fig. 2. Discrete ring variables and sign convention.

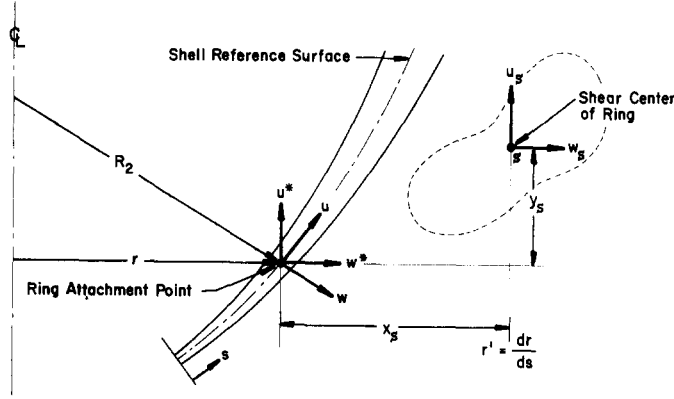


Fig. 3. Ring location relative to shell wall.

where $i = 1, 2, 3, \dots, N$ in which N is the total number of degrees of freedom in the prebuckling analysis. In eqn (3) the plastic strains $[\epsilon^P]$ and ϵ_r^P are each assumed to consist of two parts:

$$[\epsilon^P] = [\epsilon_0^P] + [\epsilon - \epsilon_0][C]^T \quad (4)$$

$$\epsilon_r^P = \epsilon_{r0}^P + (\epsilon_r - \epsilon_{r0})C_r$$

where $[C]$ and C_r are given by

$$[C] = \frac{\left\{ \frac{\partial \bar{\sigma}}{\partial \sigma} \right\} \left[\frac{\partial \bar{\sigma}}{\partial \sigma} \right] [D]}{H' + \left[\frac{\partial \bar{\sigma}}{\partial \sigma} \right] [D] \left\{ \frac{\partial \bar{\sigma}}{\partial \sigma} \right\}} \quad (5)$$

$$C_r = 1 - E_{Tr}/E_r$$

The subscript $()_0$ in eqns (4) denotes "value obtained when the material properties were last updated." In eqn (3) the quantities $[C]$, C_r , ϵ_0^P , ϵ_{r0}^P , ϵ_0 , ϵ_{r0} , ϵ^C , ϵ_r^C , ϵ^T , ϵ_r^T , $[D]$, E_r and the loads and geometrical parameters are considered to be independent of the nodal point displacements q_i .

Equation (3), then, represents a set of N nonlinear algebraic equations which are to be solved by the Newton-Raphson method. For each Newton-Raphson iteration the simultaneous linear equations

$$\sum_{j=1}^N \frac{\partial \psi_i}{\partial q_j} \Delta q_j = -\psi_i \quad i = 1, 2, \dots, N \quad (6)$$

must be solved. The elements $\partial \psi_i / \partial q_j$ in the "stiffness matrix" for each iteration have the form

$$\begin{aligned} \frac{\partial \psi_i}{\partial q_j} = & \int_{\theta} \left[\int_s \int_z \left([\epsilon] [D_T] \left\{ \frac{\partial^2 \epsilon}{\partial q_i \partial q_j} \right\} + \left[\frac{\partial \epsilon}{\partial q_i} \right] [D_T] \left\{ \frac{\partial \epsilon}{\partial q_j} \right\} \right. \right. \\ & + [[\epsilon_0][C]^T - \epsilon_0^P - \epsilon^C - \epsilon^T] [D] \left\{ \frac{\partial^2 \epsilon}{\partial q_i \partial q_j} \right\} \Big) r dz ds + \int_A \left(E_{Tr} \left(\epsilon_r \frac{\partial^2 \epsilon_r}{\partial q_i \partial q_j} + \frac{\partial \epsilon_r}{\partial q_i} \frac{\partial \epsilon_r}{\partial q_j} \right) \right. \\ & + (\epsilon_{r0} C_r - \epsilon_{r0}^P - \epsilon_r^C - \epsilon_r^T) E_r \frac{d^2 \epsilon_r}{\partial q_i \partial q_j} \Big) r dA \\ & - \int_s \left\{ -p_3 \left(\frac{1}{R_1} + \frac{1}{R_2} \right) \frac{\partial w}{\partial q_i} \frac{\partial w}{\partial q_j} + p_3 \left(\frac{1}{R_1} \frac{\partial u}{\partial q_i} \frac{\partial u}{\partial q_j} + \frac{1}{R_2} \frac{\partial v}{\partial q_i} \frac{\partial v}{\partial q_j} \right) \right. \\ & \left. \left. + \frac{dp_3}{ds} \left(\frac{\partial u}{\partial q_i} \frac{\partial w}{\partial q_j} + \frac{\partial w}{\partial q_i} \frac{\partial u}{\partial q_j} \right) \right\} r ds - \left(-V \frac{\partial^2 u_c}{\partial q_i \partial q_j} + S \frac{\partial^2 v_c}{\partial q_i \partial q_j} + H \frac{\partial^2 w_c}{\partial q_i \partial q_j} + M \frac{\partial^2 \chi}{\partial q_i \partial q_j} \right) r_c \Big] d\theta \quad (7) \end{aligned}$$

where

$$[D_T] \equiv [I - [C]^T] [D]. \quad (8)$$

Solution strategy—a double-iteration loop

The prebuckling iteration strategy is as follows: At each load level or time step there are two nested iteration loops. In the inner loop the set of simultaneous algebraic equations (6) with given fixed material properties and plastic and creep strains is solved. This is the “Newton–Raphson loop.” In the outer loop the strain-dependent quantities $[C]$, C_r , $[\epsilon_0^P]$, $\epsilon_{r,0}^P$, $[\epsilon^C]$, ϵ_r^C are calculated. Double iterations at a given load level continue until the displacements no longer change. In this way the favorable convergence property of the Newton–Raphson procedure is preserved, equilibrium is satisfied within the degree of approximation inherent in a discrete model, and the flow law of the material is satisfied at every point in the structure. A flow chart of the algorithm used in BOSOR5 is given in Fig. 2 of [1]. Nonlinear collapse can be predicted with the analysis just described.

Bifurcation buckling analysis

At a particular load equilibrium may be nonunique. Then there would exist a neighboring solution $q = q_0 + \Delta q$ which is also in equilibrium, or

$$\sum_{j=1}^M \frac{\partial \psi_i^b}{\partial q_j^b} \Big|_{q=q_0} \Delta q_j = 0 \quad i = 1, 2, \dots, M. \quad (9)$$

The superscript b indicates “buckling modal quantities” and M is the total number of degrees of freedom in the bifurcation buckling analysis. Equation (9) yields the buckled equilibrium state $\{q_0 + \Delta q\}$, since $\psi_i(q_0) = 0$ represents an equilibrium state. Equation (9) is a linear homogeneous set of equations and has a nontrivial solution only if the coefficient matrix $[\partial \psi_i^b / \partial q_j^b]$ is singular. Such singularities exist for certain values, the eigenvalues, of this stability matrix. Elements of this matrix have the form:

$$\begin{aligned} \frac{\partial \psi_i^b}{\partial q_j^b} = & \int_{\theta} \left[\int_s \int_z \left(\sigma_0 \left\{ \frac{\partial^2 \epsilon^b}{\partial q_i^b \partial q_j^b} \right\} + \left[\frac{\partial \epsilon^b}{\partial q_j^b} \right] [D_T] \left\{ \frac{\partial \epsilon^b}{\partial q_i^b} \right\} \right) r dz ds \right. \\ & \left. + \int_A \left(\sigma_{r,0} \frac{\partial^2 \epsilon_r^b}{\partial q_i^b \partial q_j^b} + E_{Tr} \frac{\partial \epsilon_r^b}{\partial q_i^b} \frac{\partial \epsilon_r^b}{\partial q_j^b} \right) r dA - \frac{\partial^2 W^b}{\partial q_i^b \partial q_j^b} \right] d\theta. \end{aligned} \quad (10)$$

in which σ_0 and $\sigma_{r,0}$ are the prebuckling stress distributions in the shell and ring, respectively and $\partial^2 W^b / \partial q_i^b \partial q_j^b$ is given by the last part of the right-hand side of eqn (7) with appropriate introduction of superscripts $()^b$ to denote buckling.

IMPLEMENTATION OF THE ANALYSIS IN THE BOSOR5
COMPUTER PROGRAM

Details such as the strain-displacement relations for shell and discrete rings are given in [1–3]. In the prebuckling analysis eqns (3)–(8) are specialized for axisymmetric deformations including moderate rotations. The row and column vectors $[\epsilon]$ and $\{\epsilon\}$ and their derivatives with respect to q_i and q_j contain two elements—the meridional and hoop strains; $[D]$, $[C]$, etc. are 2×2 matrices. Integration through the thickness of the shell is performed numerically with use of Simpson’s rule. Integration along the meridian amounts only to multiplication of the energy density by the arc length denoted “ L ” in Fig. 1, and integration over θ is replaced by multiplication by 2π .

In the nonsymmetric bifurcation buckling analysis the row and column vectors $[\epsilon^b]$ and $\{\epsilon^b\}$ contain three elements—the meridional, hoop, and in-plane shear strains; $[D]$, $[C]$, etc. are 3×3 matrices.

In BOSOR5 each discrete ring is assumed to consist of an assemblage of K straight segments of thickness T_k , length L_k , and orientation angle φ_k , $k = 1, 2, \dots, K$, as shown in Fig. 4. The material of each segment may have a different stress-strain curve and different creep properties. The temperature may vary along the length, L_k , of the ring segments, but must be constant through the thickness, T_k . The program user specifies the number of integration stations along the length of each ring segment. The integrated ring properties are determined by Simpson’s rule.

In the axisymmetric prebuckling analysis the plastic and creep circumferential strains are determined for each point in the ring cross-section exactly as described in [1] for the shell. The

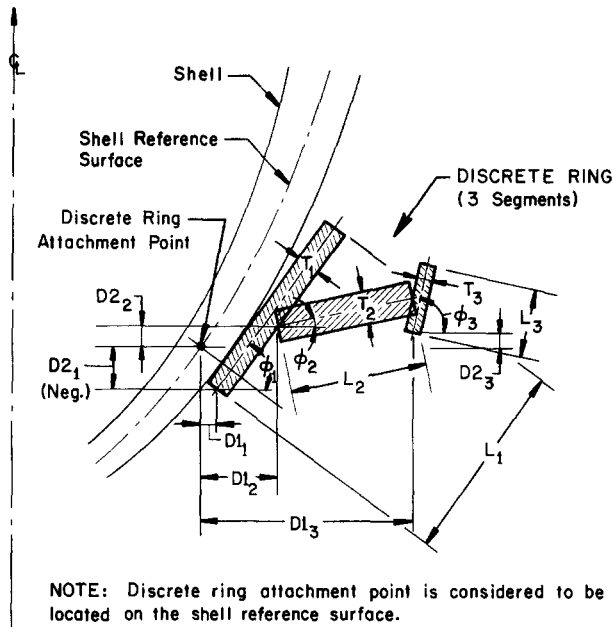


Fig. 4. Discrete ring as modeled in the BOSOR5 computer program.

implementation of the discrete ring analysis was fairly easy because the plastic and creep flow calculations for each ring segment are analogous to those for each layer through the thickness of a multi-material shell wall. The major differences are that the ring material is considered to have strength only in the circumferential direction and Poisson's ratio is assumed to be zero.

The buckling modal displacement components are assumed to vary around the circumference as $\sin n\theta$ or $\cos n\theta$ with n or a range of n being supplied by the user as input data.

The strategy to determine a bifurcation buckling load is as follows: The determinant of the stability matrix $[\partial\psi^b/\partial q^b]$ is evaluated for a particular value of circumferential wave number $n = n_{\text{start}}$ for a sequence of load or time steps until it changes sign. Then n is varied, and an eigenvalue problem of the type

$$([K_1(p_0, n)] + \lambda(n) [K_2(\Delta p, n)]) \{q(n)\} = 0 \quad (11)$$

is solved for each value of n in the range supplied by the user. $[K_1]$ is the stability matrix for the structure as loaded by p_0 , the applied load just before the change in sign of $|K_1(p, n_{\text{start}})|$. $[K_2]$ is the "load-geometric" matrix, which depends on the load step p_0 to $p_0 + \Delta p$. The critical circumferential wave number n_{cr} corresponds to the minimum $\lambda(n)$. Certain safeguards are built into the BOSOR5 computer program to avoid passing over closely spaced roots as the load is increased. These are described in the program output.

COMPARISONS WITH TESTS

In 1965 Boichot and Reynolds[4] tested 69 integrally stiffened aluminium 7075-T6 cylinders under external hydrostatic pressure. Photographs of some of the failed specimens are shown in Fig. 5, which is taken from[4]. A schematic of the geometry of all the specimens is shown in Fig. 6, with the actual dimensions given in Table 1. The stress-strain data used in the analysis are listed in Table 2.

Previous analyses applicable to some or all of these specimens have been performed by Lurchick[5], Krenzke and Kiernan[6], Reynolds[7] and Lee[8]. All of the analyses agree reasonably well with the test results, owing largely to the fact that the tangent modulus of the material decreases by more than an order of magnitude within a 20% stress range of the 0.2% yield stress.

Test results

Of the 69 test specimens, 24 have the designation "F", indicating the presence of fillets near

Table 1. Test specimen dimensions and yield strengths

Model	L_r	b	h	d	L_B	Compressive Yield Strength (0.2% Offset) psi
Dimensions in inches (See Fig. 6)						
25-88	0.699	0.127	0.0830	0.386	4.473	80,600
25-86	0.679	0.107	0.0832	0.318	4.349	80,600
25-84	0.659	0.086	0.0830	0.255	4.216	80,700
25-82	0.632	0.059	0.0826	0.179	4.047	80,700
20-88	0.572	0.112	0.0830	0.340	3.647	80,700
20-86	0.555	0.097	0.0830	0.287	3.552	80,700
20-84	0.537	0.079	0.0830	0.230	3.430	81,400
20-82	0.511	0.054	0.0832	0.158	3.280	82,000
15-88	0.444	0.100	0.0830	0.297	2.843	82,700
15-86	0.428	0.084	0.0830	0.253	2.745	82,700
15-84	0.413	0.068	0.0830	0.202	2.638	83,000
15-82	0.390	0.046	0.0830	0.140	2.502	83,300
10-88	0.313	0.084	0.0833	0.248	2.002	83,500
10-86	0.300	0.071	0.0830	0.211	1.920	83,500
10-84	0.286	0.057	0.0830	0.167	1.830	83,400
10-82	0.269	0.039	0.0833	0.115	1.715	83,200
25-58	0.532	0.086	0.0513	0.254	3.405	83,000
25-56	0.520	0.074	0.0510	0.217	3.327	83,000
25-54	0.506	0.060	0.0513	0.174	3.239	83,200
25-52	0.487	0.042	0.0511	0.123	3.117	83,400
20-58	0.434	0.077	0.0513	0.232	2.778	83,600
20-56	0.424	0.067	0.0513	0.194	2.715	83,600
20-54	0.410	0.053	0.0511	0.159	2.624	83,400
20-52	0.394	0.037	0.0511	0.110	2.522	83,300
15-58	0.337	0.069	0.0506	0.201	2.157	83,200
15-56	0.326	0.058	0.0513	0.174	2.085	83,200
15-54	0.315	0.047	0.0513	0.138	2.017	83,400
15-52	0.300	0.032	0.0514	0.097	1.919	83,500
10-58	0.235	0.057	0.0515	0.169	1.506	83,700
10-56	0.226	0.048	0.0511	0.146	1.446	83,700
10-54	0.217	0.040	0.0516	0.114	1.389	83,800
10-52	0.205	0.027	0.0518	0.078	1.311	84,100
25-28	0.320	0.043	0.0200	0.123	2.049	78,400
25-26	0.314	0.036	0.0204	0.106	2.008	80,600
25-24	0.307	0.030	0.0202	0.086	1.965	84,300
20-28	0.260	0.038	0.0203	0.111	1.661	84,300
20-26	0.253	0.032	0.0204	0.096	1.626	84,400
20-24	0.248	0.026	0.0210	0.076	1.586	84,400
15-28	0.200	0.033	0.0201	0.099	1.280	84,000
15-26	0.196	0.029	0.0205	0.081	1.254	83,800
15-24	0.190	0.023	0.0206	0.066	1.216	83,500
10-28	0.140	0.028	0.0206	0.079	0.888	83,500
10-26	0.135	0.024	0.0205	0.068	0.863	83,500
10-24	0.130	0.019	0.0203	0.056	0.834	83,600
10-22	0.124	0.014	0.0203	0.039	0.793	83,600
15-58F	0.337	0.067	0.0511	0.200	2.157	82,000
15-56F	0.325	0.056	0.0507	0.174	2.087	82,000
15-54F	0.313	0.042	0.0512	0.134	2.018	82,000
15-52F	0.300	0.030	0.0510	0.097	1.921	82,000
10-58F	0.235	0.055	0.0515	0.169	1.507	82,000
10-56F	0.225	0.047	0.0517	0.145	1.446	82,500
10-54F	0.216	0.036	0.0510	0.109	1.390	82,900
10-52F	0.205	0.025	0.0509	0.079	1.315	83,400
25-28F	0.320	0.040	0.0209	0.122	2.048	83,400
25-26F	0.310	0.030	0.0209	0.105	2.010	82,800
25-24F	0.307	0.029	0.0200	0.086	1.967	82,300
25-22F	0.298	0.019	0.0205	0.060	1.910	81,700
20-28F	0.260	0.036	0.0193	0.112	1.665	81,700
20-26F	0.253	0.030	0.0193	0.097	1.626	81,300
20-24F	0.247	0.026	0.0199	0.077	1.588	80,800
20-22F	0.241	0.018	0.0197	0.054	1.538	80,400
15-28F	0.199	0.033	0.0207	0.097	1.278	80,400
15-26F	0.196	0.028	0.0204	0.081	1.255	81,100
15-24F	0.190	0.023	0.0208	0.067	1.217	81,700
15-22F	0.183	0.016	0.0203	0.049	1.173	82,400
10-28F	0.139	0.028	0.0213	0.079	0.889	82,400
10-26F	0.137	0.027	0.0202	0.068	0.861	82,300
10-24F	0.130	0.019	0.0199	0.057	0.832	82,300
10-22F	0.125	0.015	0.0200	0.039	0.795	82,200

the boundaries and where the rings join the shell wall as indicated in Fig. 6. From the photographs in [4], it appears that practically all of the specimens without fillets fractured during failure. Figure 5 shows failure modes typical of the entire series of tests. One can see that there is considerably more fracturing of the four cylinders shown in the top half of the figure than of those shown in the bottom half. It is not possible to determine from the test data alone whether fracture caused the failure or whether fracture occurred later as the shell was deforming in its buckling mode. On the other hand, there is almost no evidence of fracture occurring in the case of the 24 specimens with fillets. Therefore, it is reasonable to predict that better agreement between test and theory will be obtained for the specimens with fillets than for those without. Furthermore, analytical predictions that are too high for the specimens without fillets would lead one to favor the hypothesis that failure was caused by fracture rather than buckling in these tests, since the analytical model is not capable of predicting fracture. This would be particularly true if the too high predictions correspond to the thicker specimens for which imperfections are less significant.

There are three different nominal radius/thickness ratios involved in the test series: $R/h \cong 12$, 20, and 50. Buckling pressures for the $R/t \cong 50$ specimens are probably somewhat sensitive to imperfections because buckling, especially of the models in this class with small ring stiffeners,

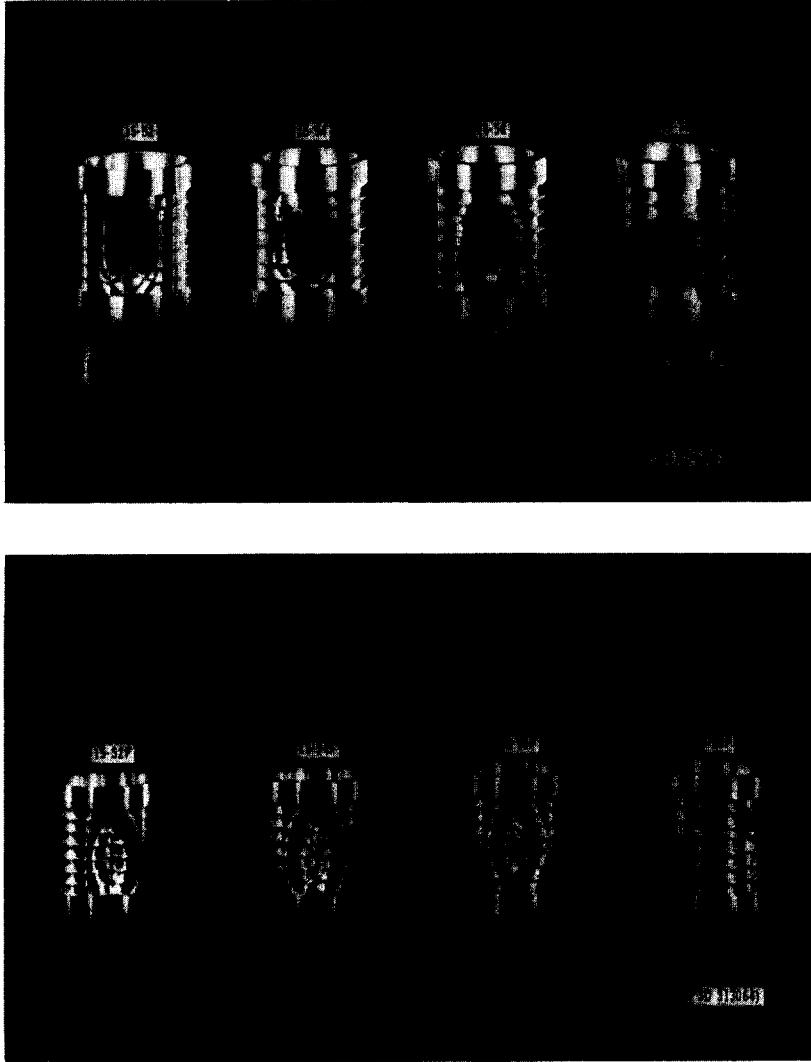


Fig. 5. Some of the buckled ring-stiffened aluminum cylinders tested under hydrostatic pressure by Boichot and Reynolds[4]: Top specimens without fillets, with evidence of fracturing; bottom, specimens of similar geometry but with fillets.

Table 2. Stress-strain relations

The following stress-strain data were used in the BOSORS analysis. These data points are derived from the formula

$$\epsilon = \frac{\sigma}{E} \left[1 + \frac{3}{7} \left(\frac{\sigma}{\sigma_y} \right)^{1.9} \right]$$

which was used by Lee [3].

Stress σ (ksi)	Strains (%) for Various σ_y (yield stress)					
	$\sigma_y = 78.4$	$\sigma_y = 80$	$\sigma_y = 81$	$\sigma_y = 82$	$\sigma_y = 83$	$\sigma_y = 84$
0.0	0.0	0.0	0.0	0.0	0.0	0.0
60.0	.5714	.5714	.5714	.5714	.5714	.5714
70.0	.6998	.6893	.6845	.6808	.6779	.6756
75.0	.8461	.8041	.7852	.7705	.7589	.7498
77.5	.9921	.9111	.8748	.8463	.8241	.8066
80.0	1.241	1.088	1.020	.9662	.9241	.8911
82.5	1.673	1.390	1.263	1.164	1.086	1.025
84.0	2.072	1.666	1.484	1.342	1.230	1.143
85.0	2.421	1.907	1.676	1.496	1.355	1.244
90.0	5.910	4.300	3.577	3.011	2.568	2.220
95.0	15.810	11.060	8.923	7.256	5.949	4.923
100.0	42.53	29.27	23.32	18.67	15.02	12.16

Material: 7075-T6 Aluminum Bar Stock

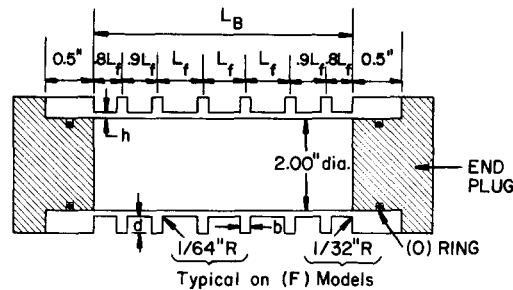


Fig. 6. Geometry of all 69 test specimens.

occurs at average stresses that are barely in the plastic range. Indeed the test results for the thinnest specimens exhibit the most scatter.

Some of the specimens in the test series buckled in an axisymmetric collapse mode and others by nonaxisymmetric bifurcation buckling. The BOSOR5 code calculates either mode of failure, whichever corresponds to the lowest pressure.

Determination of the Best Analytical Model

Figure 6 shows a schematic of the actual test specimen with rigid end plugs. Previous analyses [7, 8] have assumed equally spaced rings and simple support at the interior faces of the end plugs. In the present effort a preliminary parameter study on one of the test specimens was made with BOSOR5 in order to determine the best analytical model prior to treatment of all 69 specimens.

Specimen 10-52F was chosen as the standard of comparison because very good agreement between test and theory is to be expected in this case for the following reasons:

1. The presence of fillets apparently eliminated the fracture mode of failure. From the photograph in [4] of the buckled specimen, it is clear that the mode of failure was general nonaxisymmetric instability.

2. The shell was quite thick ($R/t = 20$), leading to small sensitivity to imperfections for the following reasons: (i) The thicker shells buckled at average stresses well above the proportional limit of the material. Since the tangent modulus of the material varies rapidly in the stress region corresponding to the buckling pressure, the deleterious effect of imperfections is "buffered" by the resulting increase in the tangent modulus at the lower level of average critical stress for the imperfect shell. (ii) The effect of an imperfection is related to the amplitude of the imperfection divided by the shell thickness. A given tolerance on out-of-roundness existed for all 69 specimens. Therefore the geometrical imperfections in the thicker shells reduce their buckling pressures by smaller percentages than is the case for the thinnest shells.

3. For certain cases it is necessary to account for the fact that the ring thickness represents a rather large percentage of the length of shell between rings. The cylinder is not as free to bend meridionally in the region of the ring-shell intersection as it is elsewhere. Therefore, strictly speaking, it is not correct to consider the discrete rings to be attached to the shell at a single point and to be free to bend meridionally in the immediate neighborhood of this point. For Specimen 10-52F, however, this ring thickness effect is small for two reasons: The ring thickness actually was a rather small percentage of the ring spacing, and the failure mode was general instability for which this ring thickness effect is very small.

Figure 7 is a schematic of Specimen 10-52F. Half of the shell is represented with symmetry conditions being imposed at the symmetry plane. The rigid end plug is simulated by three rigid supports which permit axial sliding in the prebuckling phase of the problem but which do not permit normal deflection or meridional rotation. Nodal points are densely packed near the thick Segment 1, where local axial bending strains are very high and changing steeply with axial coordinate. The discrete rings are considered to be attached at single nodal points, labeled 16, 25, and 36 in Fig. 7.

Table 3 gives the results of a parameter study in which various modifications of this analytical model were treated with use of BOSOR5. Critical pressure ranges are listed because it is known only that the stability determinant changes sign between the values given.

Case 7 leads to a prediction within 1% of the critical pressure determined from the test. It was

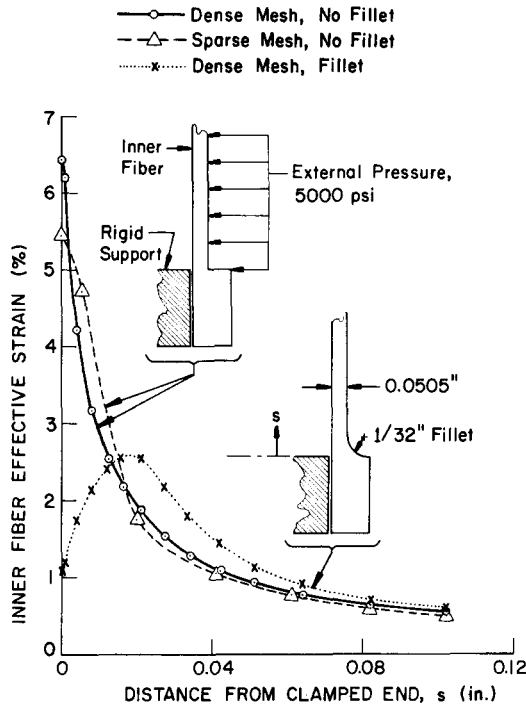


Fig. 8. Effective strain near edge for Specimen 10-52F at 5000 psi analyzed with and without edge fillet.

Table 3. Parameter study of specimen 10-52F to determine the best analytical model of all specimens

CASE	ANALYTICAL MODEL	BOUNDARY CONDITIONS USED IN THE STABILITY ANALYSIS TO SIMULATE THE END PLUG (Prebuckling boundary conditions were the same for all cases)	PREDICTED CRITICAL PRESSURE RANGE IN PSI (CIRC. WAVENUMBER)
1	As shown in Figure 7.	Axial (u) and circumferential (v) sliding permitted, normal deflection (w) and meridional rotation (χ) restrained	5060-5080(4)
2	As shown in Figure 7, except rings treated as flexible shell branches	Same as Case 1	5060-5080(4)
3	As shown in Figure 7, except rings "smeared" as described in [9]	Same as Case 1	5060-5080(4)
4	As shown in Figure 7, except variable thickness near support simulating the fillet shown in Figure 4.	Same as Case 1	5080-5100(4)
5	Same as Case 4, except boundary conditions	Clamped at end plug (u,v,w,χ = 0)	5140-5160(5)
6	As shown in Figure 7, except nodal points not concentrated at beginning of Seg. 2. Eight equal intervals between end plug and discrete ring #1, each 0.1 L _p long.	Clamped at end plug	5140-5160(5)
7	Segment 2 only, with nodal point distribution as in Case 1	Clamped at end plug	5140-5160(5)

Critical test pressure for this specimen was 5099 psi

the prebuckled state in the edge region are doubtless not very accurate. Shell theory is just not sufficient to calculate details of the actual local edge deformations which must involve considerable transverse shearing. Thus, the present analysis does not lead to a definite conclusion that in the tests of the specimens without fillets fracture preceded buckling. However, because of the high strains obtained in this analysis, our belief is reinforced that many of the specimens did indeed fail by fracturing and not by buckling.

Comparison with all the tests

Tables 4 and 5 and Fig. 9 give the test pressures and BOSOR5 predictions with use of the analytical model identified as Case 7 in Table 3. Each of the 69 examples involves approximately 90 degrees of freedom in the prebuckling analysis and 130 degrees of freedom in the stability analysis. About three minutes of UNIVAC 1110 computer time were required for execution of

Table 4. Comparison of test & theory for buckling of models without fillets

Model	Observed Buckling Pressure (psi)	Adjusted Pressure (psi)	BOSOR5 Prediction (psi)	Adjusted BOSOR5	Buckling Mode (No. of Circ.Waves)	b/\sqrt{Rt}
25-88	9450	9875	9170	1.077	0	.431
25-86	9550	9980	9310	1.072	0	.363
25-84	8850	9237	9400	0.983	0	.293
25-82	7275	7593	8400	0.904	3	.200
20-88	10600	11062	10080	1.098	0	.380
20-86	9750	10176	10240	0.994	0	.329
20-84	8800	9105	9900	0.920	3	.269
20-82	7400	7696	8490	0.906	3	.184
15-88	11600	12105	11760	1.029	0	.340
15-86	10000	10435	11280	0.925	3	.286
15-84	9100	9462	10080	0.939	3	.231
15-82	7650	7926	8660	0.915	4	.156
10-88	12100	12658	13000	0.974	0	.284
10-86	10650	11140	11500	0.969	3	.242
10-84	9150	9468	10120	0.935	4	.193
10-82	7650	7937	8750	0.907	4	.133
25-58	5600	5740	5725	1.003	0	.373
25-56	5600	5739	5750	0.998	0	.322
25-54	5550	5678	5820	0.976	0	.263
25-52	4470	4559	5200	0.877	3	.182
20-58	6300	6488	6375	1.017	0	.335
20-56	6300	6488	6440	1.007	0	.292
20-54	5450	5559	6150	0.904	3	.231
20-52	4500	4595	5260	0.874	4	.161
15-58	7050	7205	7080	1.018	0	.300
15-56	6400	6544	6950	0.942	3	.253
15-54	5500	5610	6240	0.899	4	.205
15-52	4600	4742	5320	0.891	4	.140
10-58	7250	7458	7875	0.947	0	.248
10-56	6450	6634	7080	0.937	4	.209
10-54	5625	5779	6280	0.920	4	.174
10-52	4700	4812	5340	0.901	5	.118
25-28	1850	1868	1920	0.973	0	.298
25-26	1960	1990	2080	0.956	0	.249
25-24	1880	1892	2120	0.893	0	.207
20-28	2225	2239	2340	0.957	0	.264
20-26	2150	2162	2380	0.908	0	.222
20-24	2075	2085	2360	0.884	0	.181
15-28	2400	2424	2620	0.925	0	.229
15-26	2360	2389	2560	0.933	0	.202
15-24	2060	2093	2350	0.891	5 ^a	.160
10-28	2625	2666	2800	0.952	0	.194
10-26	2360	2398	2590	0.925	0	.167
10-24	2040	2070	2340	0.885	6	.132
10-22	1640	1664	1920	0.867	6	.097

^aBuckling mode is antisymmetric at symmetry plane.

Table 5. Comparison of test & theory for buckling of models with fillets

Model	Observed Buckling Pressure (psi)	Adjusted Pressure (psi)	BOSOR5 Prediction (psi)	Adjusted BOSOR5	Buckling Mode (No. of Circ.Waves)	b/\sqrt{Rt}
1558F	7400	7584	7060	1.074	0	.292
1556F	6750	6917	6800	1.017	3	.244
1554F	5850	5999	5920	1.013	4	.183
1552F	4920	5042	5140	0.981	4	.131
1058F	7700	7897	7620	1.036	0	.240
1056F	6800	7013	6940	1.011	4	.205
1054F	5950	6105	5940	1.028	4	.157
1052F	5000	5099	5140	0.992	5	.109
2528F	2160	2172	2160	1.005	0	.278
2526F	2080	2106	2180	0.966	0	.209
2524F	1935	1947	2060	0.945	0	.200
2522F	1420	1439	1600	0.900	4	.133
2028F	2135	2164	2260	0.957	0	.249
2026F	2100	2113	2140	0.987	0	.207
2024F	2060	2086	2180	0.957	0	.180
2022F	1520	1527	1700	0.893	5	.126
1528F	2580	2606	2620	0.995	0	.230
1526F	2400	2421	2460	0.984	0	.195
1524F	2180	2210	2250	0.982	5 ^a	.160
1522F	1720	1729	1840	0.939	5	.111
1028F	2840	2854	2680	1.065	0	.194
1026F	2540	2556	2560	0.998	0	.188
1024F	2180	2194	2280	0.962	5	.132
1022F	1775	1788	1880	0.951	6	.104

^aBuckling mode is antisymmetric at the symmetry plane.

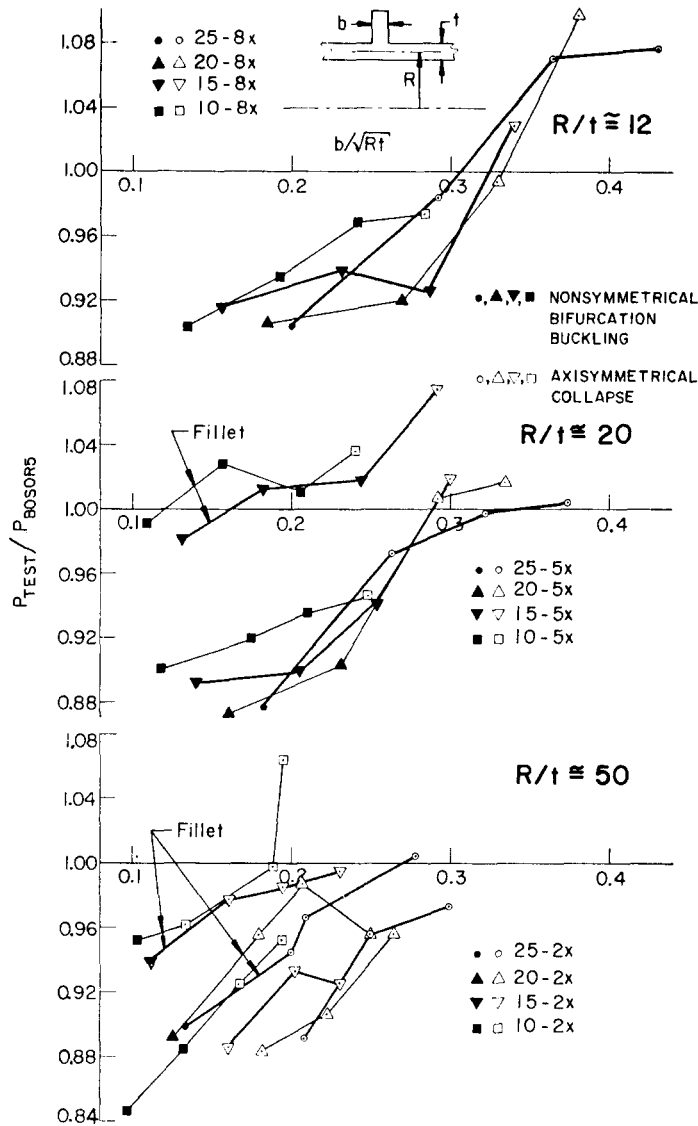


Fig. 9. Comparison of test and theory with use of analytical model identified as Case 7 in Table 3, plotted as function of ring thickness parameter, b/\sqrt{Rt} .

each case. The lowest buckling pressure corresponds to a buckling mode which is symmetric about the symmetry plane in all except two cases—Specimens 15-24 and 15-24F. In these two cases the critical mode is antisymmetric about the symmetry plane. The buckling pressures corresponding to a buckling mode which is symmetrical about the symmetry plane are very slightly higher—2360 psi for Specimen 15-24 and 2260 psi for Specimen 15-24F.

In Tables 4 and 5 the adjusted pressure is approximately the observed pressure, which acts on the outer surface of the shell, multiplied by the ratio of the outer surface radius to the middle surface radius. Another factor, slightly different from unity, is applied to adjust for the differences between the observed yield stresses listed in Table 1 and the rounded values of yield stress used to generate the stress-strain data given in Table 2. A buckling mode with zero circumferential waves indicates that the predicted failure is due to axisymmetric collapse rather than bifurcation buckling. The analysis predicts that more of the cylinders failed in this mode than the photographs of [4] seem to indicate. There are two probable reasons for this discrepancy between theory and test:

1. In many cases the axisymmetric and nonaxisymmetric modes of failure occur at almost the same pressure. A slight imperfection, while not much affecting the critical pressure, might easily cause a nonaxisymmetric buckling pattern to develop during the post-buckling process. In the

photograph of [4] are seen the far post-buckled states of the specimens, not the initial buckling modes.

2. The analytical model used to generate the predictions in Tables 4 and 5 underestimates the axisymmetric collapse mode of failure because the discrete rings are considered to be attached to the shell at single meridional points with the shell being free to bend axially within the thickness b of each ring. This effect is particularly important for the specimens with larger values of b/\sqrt{Rt} . It will be evaluated quantitatively in the following section.

Figure 9 shows the tabulated results plotted versus the ring thickness ratio b/\sqrt{Rt} . The three frames correspond to the three nominal R/t values, $R/t = 12$ in the top frame, 20 in the middle frame and 50 in the bottom frame. Each point corresponds to a single test specimen. The points designated "Fillet" are from Table 5.

The generally upward sloping trend results primarily from the fact that the analytical model becomes increasingly conservative with increasing b/\sqrt{Rt} : The neglected effect on the shell meridional bending stiffness of the finite thicknesses of the rings leads to a prediction of axisymmetric collapse with relatively short axial wavelengths. Actually, this mode is hindered by the increased local meridional bending stiffness afforded by the finite axial intersection lengths of shell and rings.

There is a greater degree of scatter apparent in the case of the thinnest specimens, which are somewhat susceptible to the presence of initial imperfections.

Table 6 gives comparisons with analyses by Reynolds [7] and Lee [8] for all the specimens for which analytical results are available from [7] and [8]. The BOSOR5 results are higher than those obtained by Lee and Reynolds. The reasons for the discrepancy are not known at present.

Analysis of the ring thickness effect

With use of BOSOR5, it is possible to investigate analytically the effect on predicted critical pressures of including some additional axial bending stiffness due to the finite axial length of the shell-ring intersection areas. This increase in axial bending rigidity is modeled as shown in Fig. 10. Additional mesh points are provided in the neighborhoods of the discrete rings with meridional rotation constrained to be equal at nodal points corresponding to the bottom and top surfaces of each discrete ring. The solid line, labeled Model 1, corresponds to the original analytical models of the test series 15-5XF in which the discrete ring is considered to be attached at one point and the shell is free to bend under the ring. That is, the prebuckling meridional rotation χ is free to change along the shell wall within the shell-ring intersection area. With the extra constraint conditions (Model 2) the analytical predictions are closer to the test results. The critical failure mode for the specimen with the thickest rings, Specimen 15-58F for which $b/\sqrt{Rt} \cong 0.3$, is predicted to be axisymmetric inter-ring collapse with use of Model 1 and nonsymmetric general instability with use of Model 2. In the cases for which general nonaxisymmetric instability is predicted with use of Model 1, introduction of extra constraint conditions as depicted in Fig. 10 does not change the prediction very much. Analytical results for all of the cases investigated with

Table 6. Comparison with other analyses

Model	P_{test} (Adjusted)	$P_{\text{BOSOR5}}(n)^a$	$P_{\text{LEE}}(n)^b$	$P_{\text{REYNOLDS}}(n)^c$
10-52	4812	5340(5)	4670(3)	4779(5)
10-54	5779	6280(4)	5915(3)	5270(4)
10-82	7937	8750(4)	7521(2)	7786(4)
10-88	12658	13000(0)	10440(5)	11503(3)
15-82	7926	8660(4)	7647(2)	7663(3)
15-84	9462	10080(3)	8331(9)	8654(3)
15-88	12105	11760(0)	10987(4)	11166(3)
20-82	7696	8490(3)	7687(2)	7556(3)
20-84	9105	9900(3)	8131(7)	8390(3)

^a n = number of circumferential waves in buckling mode.

^b Reference [8]

^c Reference [7]

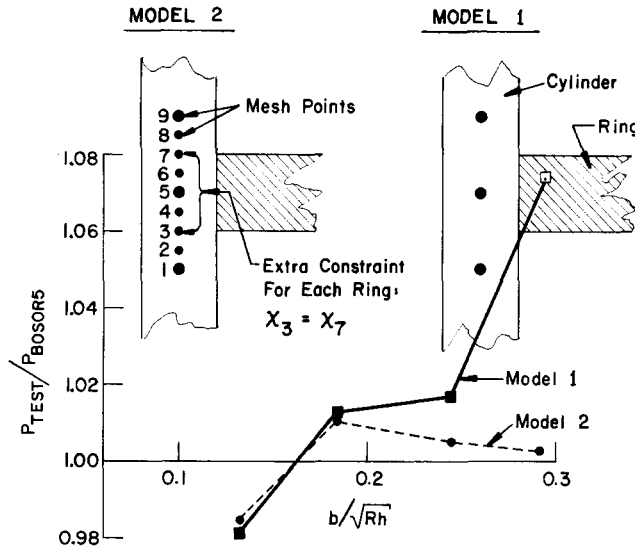


Fig. 10. Comparison of test and theory for Specimens 15-5XF neglecting and including ring thickness effect.

use of Model 2 are given in Table 7. Unfortunately, the budget for computer time did not permit analysis of the entire series of tests with use of Model 2.

Figure 11 shows the predicted axisymmetric failure modes for Specimen 25-88 with use of Model 1 and Model 2 analysis. It is clear from these plots why introduction of the extra constraint conditions raises the axisymmetric collapse load.

Conclusions

In general the test results and analytical results are in reasonably good agreement. Because of the shape of the stress-strain curve, one would not expect most of the specimens to be sensitive to imperfections. Nor would one expect much sensitivity of the predicted critical pressures to changes in the analytical model such as nodal point density, boundary conditions, and treatment of ring stiffness.

It appears from the results obtained in this study that most or all of the test specimens without fillets failed by fracturing rather than by buckling. However, shell theory cannot predict accurately the local strain concentrations at the rings or at the edges. A more elaborate analysis of these areas, perhaps a modeling of them by means of two-dimensional grids of axisymmetric finite elements, will have to be made if this problem is to be solved with more certainty.

The results indicate that the buckling pressures of the thinnest shells ($R/t \cong 50$) are somewhat sensitive to imperfections, mainly because there is little plastic flow prior to buckling. If one

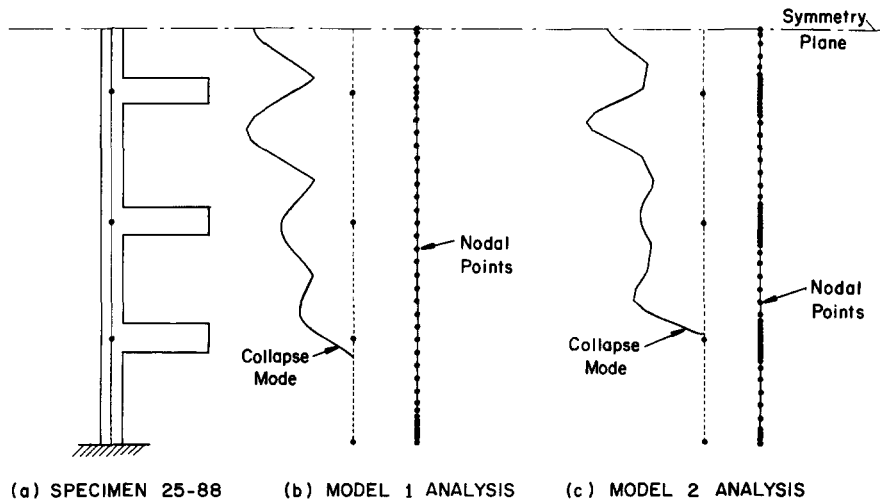


Fig. 11. Predicted axisymmetric collapse modes of Specimen 25-88: (a) Specimen geometry, (b) neglecting ring thickness effect, (c) including ring thickness effect.

restricts one's attention only to those specimens which definitely did not fracture and which are not sensitive to imperfections, then the agreement between test and theory is very good. However, only eight of the 69 specimens fall into this class—the four designated 10-5XF and the four designated 15-5XF. From Table 7 it is seen that the maximum discrepancy between test and theory for those specimens is 3.6% if the ring thickness effect is included in the analytical model.

Table 7. Comparison of two analytical models with test results

SPECIMEN	b//RE	ADJUSTED TEST PRESSURE (psi)	TEST	
			MODEL 1	MODEL 2
25-88	.431	9875	1.077(0)	0.946(0)
25-86	.363	9980	1.072(0)	0.975(0)
25-84	.293	9237	0.983(0)	0.944(2)
25-82	.200	7593	0.904(3)	0.908(3)
15-58F	.292	7584	1.074(0)	1.003(3)
15-56F	.244	6917	1.017(3)	1.005(3)
15-54F	.183	5999	1.013(4)	1.013(4)
15-52F	.131	5042	0.981(4)	0.985(4)
10-58F	.240	7987	1.036(0)	1.036(3)
10-56F	.205	7013	1.011(4)	1.011(4)
10-54F	.157	6105	1.028(4)	1.028(4)
10-52F	.109	5099	0.992(5)	0.992(5)
10-28F	.194	2854	1.065(0)	0.998(0)
10-26F	.188	2556	0.998(0)	0.975(0)
10-24F	.132	2194	0.962(5)	0.979(6)
10-22F	.104	1788	0.951(6)	0.944(6)

REFERENCES

1. D. Bushnell, Large deflection elastic-plastic creep analysis of axisymmetric shells, *Numerical Solution of Nonlinear Structural Problems*, AMD-Vol. 6. Presented at the ASME Winter Annual Meeting, Detroit, Michigan, Nov. 1973, (Editor, R. F. Hartung), pp. 103-138 (1973).
2. D. Bushnell, Bifurcation buckling of shells of revolution including large deflections, plasticity and creep. *Int. J. Solids Structures*, **10**, 1287 (1974).
3. D. Bushnell, *BOSOR5—A Computer Program for Buckling of Elastic-Plastic Complex Shells of Revolution Including Large Deflections and Creep*, Vol. I: *User's Manual, Input Data*, LMSC D407166; Vol. II: *User's Manual, Test Cases*, LMSC D407167; Vol. III: *Theory and Comparisons with Tests*, LMSC D407168. Lockheed Missiles & Space Co., Sunnyvale, Ca., (Dec. 1974).
4. L. Boichot and T. E. Reynolds, Inelastic buckling tests of ring-stiffened cylinders under hydrostatic pressure. *David Taylor Model Basin Report 1992*, Washington, D.C. (May 1965).
5. M. E. Lurchick, Plastic general instability of ring-stiffened cylindrical shells. *David Taylor Model Basin Report 1587*, Washington, D.C. (Sept. 1963).
6. M. A. Krenzke and T. J. Kiernan, Structural development of a titanium oceanographic vehicle. *David Taylor Model Basin Report 1675*, Washington, D.C. (Sept. 1963).
7. T. E. Reynolds, Private Communication (June 1974).
8. L. H. N. Lee, Inelastic asymmetric buckling of ring-stiffened cylindrical shells under external pressure. *AIAA J.* **12**, 1051 (1974).
9. G. Gerard, Plastic stability theory of stiffened cylinders under hydrostatic pressure. *J. Ship Res.* **6**, 1 (1962).
10. G. A. Cohen, Conservativeness of a normal pressure field acting on a shell. *AIAA J.* **4**, 1886 (1966).